ACS NANO
Cite This: ACS Nano 2019, 13, 10036−10048
www.acsnano.org

ARTICLE

Synthesis and High-Pressure Mechanical Properties of Superhard Rhenium/Tungsten Diboride Nanocrystals

Jialin Lei,[†] Shanlin Hu,[†] Christopher L. Turner,[†] Keyu Zeng,[†] Michael T. Yeung,[†] Jinyuan Yan,[∥] Richard B. Kaner,[*,†,‡,§] and Sarah H. Tolbert[*,†,‡,§]

[†]Department of Chemistry and Biochemistry, UCLA, Los Angeles, California 90095-1569, United States
[‡]Department of Materials Science and Engineering, UCLA, Los Angeles, California 90095-1595, United States
[§]California NanoSystems Institute (CNSI), UCLA, Los Angeles, California 90095, United States
[∥]Advanced Light Source, Lawrence Berkeley National Lab, Berkeley, California 94720, United States

Supporting Information

ABSTRACT: **Rhenium diboride is an established superhard compound that can scratch diamond and can be readily synthesized under ambient pressure. Here, we demonstrate two synergistic ways to further enhance the already high yield strength of ReB_2. The first approach builds on previous reports where tungsten is doped into ReB_2 at concentrations up to 48 at. %, forming a rhenium/tungsten diboride solid solution ($Re_{0.52}W_{0.48}B_2$). In the second approach, the composition of both materials is maintained, but the particle size is reduced to the nanoscale (40−150 nm). Bulk samples were synthesized by arc melting above 2500 °C, and salt flux growth at ∼850 °C was used to create nanoscale materials. *In situ* radial X-ray diffraction was then performed under high pressures up to ∼60 GPa in a diamond anvil cell to study mechanical properties including bulk modulus, lattice strain, and strength anisotropy. The differential stress for both $Re_{0.52}W_{0.48}B_2$ and nano ReB_2 (n-ReB_2) was increased compared to bulk ReB_2. In addition, the lattice-preferred orientation of n-ReB_2 was experimentally measured. Under non-hydrostatic compression, n-ReB_2 exhibits texture characterized by a maximum along the [001] direction, confirming that plastic deformation is primarily controlled by the basal slip system. At higher pressures, a range of other slip systems become active. Finally, both size and solid-solution effects were combined in nanoscale $Re_{0.52}W_{0.48}B_2$. This material showed the highest differential stress and bulk modulus, combined with suppression of the new slip planes that opened at high pressure in n-ReB_2.**

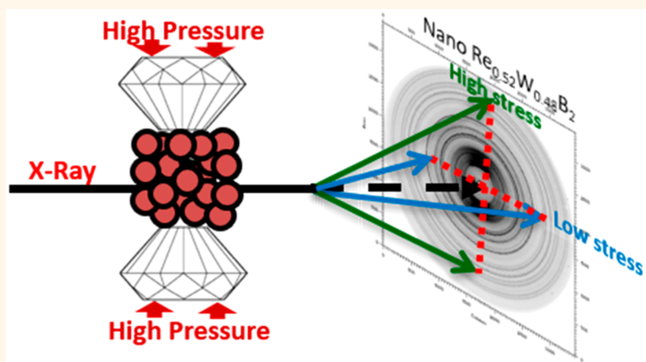

KEYWORDS: *superhard, ultra-incompressible, transition metal borides, nanocrystal, radial diffraction, lattice-preferred orientation, elastic and plastic deformation*

As new state-of-the-art materials and metals are discovered and synthesized, the demand for materials capable of cutting, forming, and shaping those new materials grows. Diamond, the world's hardest natural material, cannot be effectively used for cutting and drilling ferrous metals because of its poor thermal stability in air and its tendency to form carbides.[1−3] Cubic boron nitride (c-BN), an alternative to diamond, is of interest because of its high hardness and excellent chemical stability,[4] but high pressure is necessary to synthesize c-BN, which again limits its use. In 2007, rhenium diboride (ReB_2) was successfully synthesized by arc melting at ambient pressure.[5] ReB_2 shows a third-order bulk modulus of 340 GPa[6] and a Vickers hardness (H_v) as high as 40.5 GPa[7] under an applied load of 0.49 N. Although its hardness value only narrowly surpasses the threshold for superhard materials (H_v > 40 GPa), it is still capable of scratching a natural diamond.[8]

It has been reported that the hardness of ReB_2 can be increased to ∼48 GPa *via* solid solution hardening (*i.e.*, $Re_{1-x}W_xB_2$) where tungsten is added into the host lattice.[9] Interestingly, pure tungsten diboride (WB_2) has been shown to be ultra-incompressible, but not superhard,[10−15] because it takes a crystal structure that is intermediate between that of

Received: March 18, 2019
Accepted: July 31, 2019
Published: August 2, 2019

DOI: 10.1021/acsnano.9b02103
ACS Nano 2019, 13, 10036−10048

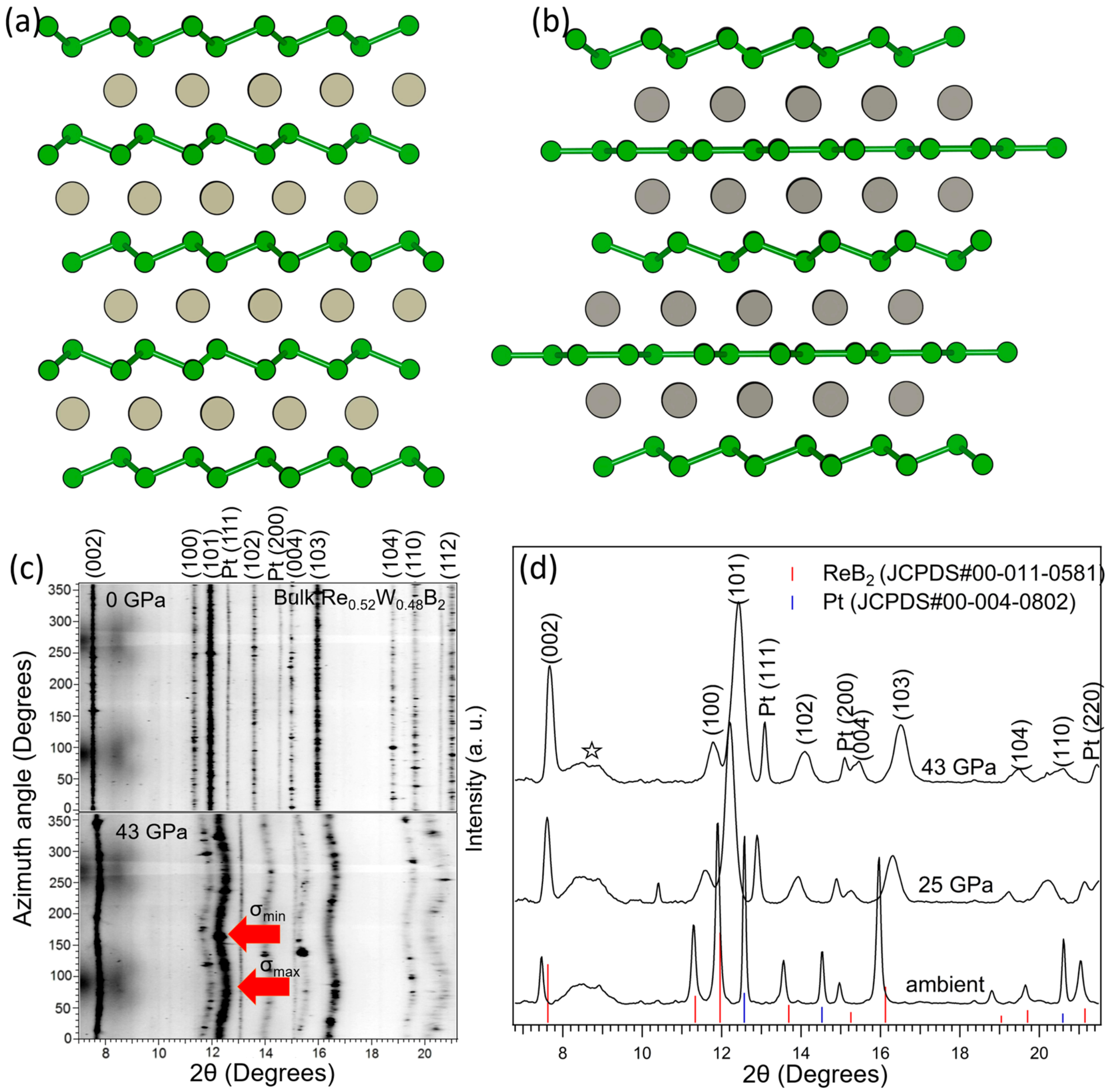

Figure 1. Comparison of the structures of ReB_2 (a) and WB_2 (b). Boron and metal atoms are shown in green and gray, respectively. Representative synchrotron 2-D azimuthally unrolled patterns (c) and 1-D X-ray diffraction patterns (d) with increasing pressure for bulk $Re_{0.52}W_{0.48}B_2$. The data in part (d) were obtained by integration over a 5° slice centered at the magic angle of φ = 54.7°. Indexing for relevant peaks is included on the image (note that the stick pattern is for ReB_2, not $Re_{0.52}W_{0.48}B_2$). Diffraction from the boron/epoxy gasket is indicated with an open star. All diffraction peaks other than those from the gasket shift to higher angle with increased pressure.

ReB_2 (*P*6$_3$*/mmc*, containing corrugated boron layers alternating with metal layers; Figure 1a) and AlB_2 (*P*6*/mmm*, containing flat boron sheets, again alternating with metal layers). The WB_2 structure consists of alternating corrugated and planar boron sheets (Figure 1b). The presence of any planar boron sheets provides easy slip planes and significantly reduces the hardness of the material. We have previously shown that the ReB_2-type structure can be maintained with tungsten content up to 48 at. % for $Re_{1-x}W_xB_2$ solid solutions, providing a large window for solid solution-based hardness enhancement.[9]

While we have found that crystal engineering to tune the intrinsic hardness of a material is an excellent method to enhance hardness, in many cases extrinsic effects, such as finite size or multiphase effects, can produce even greater enhancement. It turns out that the extremely high hardness in $W_{0.92}Zr_{0.08}B_4$ (H_v = 55 GPa) and $W_{0.99}Re_{0.01}B_4$ (H_v = 50 GPa) can be explained by morphological control and secondary phase dispersion hardening, respectively.[16,17] One would expect that a higher hardness for ReB_2 can be achieved by reducing its grain size, known as the Hall−Petch effect. Indeed, work in other nanoscale systems has shown fantastic enhancements. Chen *et al.* have demonstrated that the stress-induced dislocation activity can be suppressed to a significant extent for 3 nm Ni nanocrystals.[18] Although Ni metal is not superhard, it provides insights for the potential to tune mechanical properties by changing slip systems. The challenge is that forming nanostructured superhard materials is still

DOI: 10.1021/acsnano.9b02103
ACS Nano 2019, 13, 10036−10048

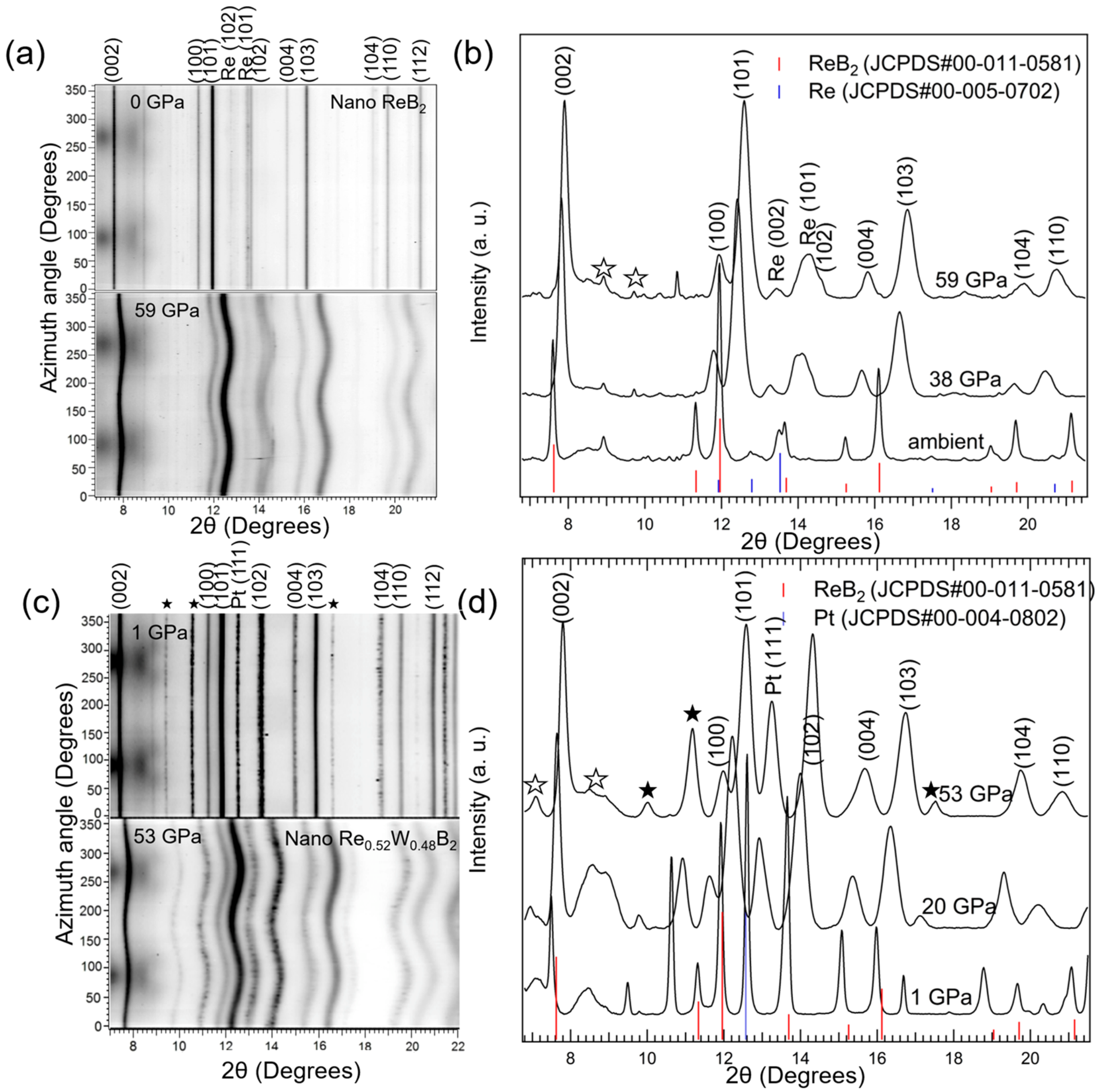

Figure 2. Representative synchrotron 1-D X-ray diffraction patterns and 2-D azimuthally unrolled patterns with increasing pressure for (a, b) nano-ReB_2 and (c, d) nano-$Re_{0.52}W_{0.48}B_2$. The data in parts (b) and (d) were obtain by integration over a 5° slice centered at the magic angle of φ = 54.7°. Indexing for relevant peaks is included on the image (note that the stick pattern is for ReB_2, in both figures). Diffraction from the boron/epoxy gasket is indicated with an open star and an impurity in the n-$Re_{0.52}W_{0.48}B_2$ is labeled with a closed star. All diffraction peaks other than those from the gasket shift to higher angle with increased pressure.

synthetically difficult. Mechanical grinding below the micrometer scale is extremely challenging for superhard materials. All reported synthetic routes to nanocrystalline superhard materials typically require applied pressure in gigapascals. Nanotwinned c-BN has been prepared under a pressure of 15 GPa by using an onion-like BN as the precursor, and this material showed unparalleled hardness.[19] Similarly, nanotwinned diamond was synthesized at 20 GPa and 2000 °C using a high-energy metastable carbon as the precursor, and the resultant materials had a Vickers hardness as high as 200 GPa.[20]

A bottom-up synthetic route to nanoscale transition metal borides based on $Sn/SnCl_2$ redox chemistry was recently reported.[21] Here, elemental boron and anhydrous metal chlorides were mixed with Sn in a glovebox and sealed in a quartz ampule under vacuum. This was followed by heat treatment between 700 and 900 °C. A variety of transition metal borides with the general composition of M_xB_y (x, y = 1−4), where M is a 3d, 4d, or 5d element, can be made through this method, such as TaB_2, NbB_2, Mo_2B, and MoB_2. Portehault *et al.* also reported a general solution route toward metal boride nanocrystals using solid metal chlorides and sodium borohydride as metal and boron sources.[22] A LiCl/KCl eutectic was chosen as the flux. Various systems ranging from hexaborides to monoborides such as CaB_6, MoB_4, NbB_2, and FeB were synthesized to demonstrate the generality of this

DOI: 10.1021/acsnano.9b02103
ACS Nano 2019, 13, 10036−10048

approach. However, many of the superhard members of the metal boride family have yet to be explored.

As discussed above, all superhard nanocrystals reported to date have been synthesized under high pressure. Here, we report a synthetic approach to make nanocrystalline versions of the superhard materials ReB_2 (n-ReB_2) and $Re_{0.52}W_{0.48}B_2$ (n-$Re_{0.52}W_{0.48}B_2$) *via* molten salt flux growth at ambient pressure. We then use synchrotron-based angle dispersive X-ray diffraction (XRD) experiments in a radial geometry using a diamond anvil cell (DAC)[23] to determine the bulk modulus of these new materials and to examine the differential stress in a lattice plane specific manner up to ∼60 GPa. The differential stress has been commonly considered as a good estimate of yield strength in many studies, and it is found to strongly correlate to hardness.[24−30] Differential stress can only be measured through radial diffraction, where the sample is compressed non-hydrostatically, rather than the traditional axial diffraction, where a hydrostatic pressure medium[31] is employed. Radial diffraction studies have the added benefit that very small sample volumes are needed and that powders can be studied directly, without the need for first compacting them.

Another advantage for radial diffraction over axial diffraction is that texture in the radial geometry is sensitive to the active slip systems as well as stress,[32−34] which enables elucidation of the microscopic deformation mechanisms controlling the plastic behavior of the material.[18,35] Through an understanding of the mechanisms by which available slip systems are tuned, we have the potential to rationally design the next generation of ultrahard metal borides. Such ideas have been used previously for a range of superhard metal borides. For example, Yeung *et al.* found that the intrinsic yield strength of tungsten monoboride could be dramatically improved by removing the slip plane through selective substitution of the malleable tungsten bilayer with Ta.[29,30,36] This substitution pushes the originally nonsuperhard boride into the superhard regime, demonstrating an effective design strategy. Although there are theoretical calculations predicting the slip systems for ReB_2,[37−39] to date there are no papers where lattice-preferred orientation and deformation mechanisms under high pressure are experimentally investigated.

In this work, we combine all of these ideas to examine how both finite size effects and solid-solution formation can be used to enhance hardness in a family of materials based on ReB_2. Radial diffraction is used instead of indentation hardness, because solid compacts of the nanocrystal-based materials have not been fabricated and so these materials are not amenable to traditional hardness measurements. Because of the high quality of nanocrystal-based powder diffraction, however, we are able to extract a much higher level of information from the radial diffraction, gaining insight into both the bulk slip systems and the effect of atomic substitution on those slip systems. We specifically compare bulk ReB_2 with n-ReB_2 to examine size effects. We then compare bulk ReB_2 with bulk $Re_{0.52}W_{0.48}B_2$ in mechanical properties to examine how solid solutions can enhance hardness. Finally, we combine these two approaches in nanoscale $Re_{0.52}W_{0.48}B_2$ (n-$Re_{0.52}W_{0.48}B_2$) to examine the synergistic effects of using both finite size effects and solid-solution hardening. In the future, spark plasma sintering (SPS) will be adopted to produce a solid bulk compact of nanocrystals. Because of its very high heating rate, this rapid sintering process may avoid excessive coarsening and therefore maintain the outstanding mechanical properties of these nanocrystals into practical bulk materials.

RESULTS AND DISCUSSION

Previous synthetic efforts have explored reactions between metal halides and sodium borohydride to produce transition metal boride nanocrystals, mainly based on redox chemistry, where the alkali borohydrides serve as both reductant and boron source.[21,22] In contrast, our synthesis of nano-ReB_2 and $Re_{0.52}W_{0.48}B_2$ employed elemental Re and boron to limit impurities. The operative mechanism in our synthesis is closer to the classical solid-state method, where the diffusion of boron into the metal lattice is likely assisted by the molten salt flux. In the synthesis of nanomaterials, the ratio of metal to boron was kept at 1:4. The excess boron is very important for the synthesis of ReB_2 from the elements, as diffusion of boron into the metal lattice to achieve the correct stoichiometry is driven by the presence of excess boron. Indeed, the addition of excess boron is also very common in the synthesis of bulk transition metal borides made by conventional high-temperature routes and is particularly important for superhard borides to thermodynamically drive the formation of phase-pure materials. For example, WB_4 is typically made at a metal to boron ratio of 1:12.[17] Dodecaborides such as ZrB_{12} and YB_{12} are generally made at a ratio of 1:20.[40] Fortunately, in the radial diffraction experiment, differential strain is measured in a lattice-specific manner, and so any extra boron content does not negatively influence the analysis.

In situ XRD studies were conducted under non-hydrostatic compression up to ∼60, 43, and 53 GPa for n-ReB_2, bulk $Re_{0.52}W_{0.48}B_2$, and n-$Re_{0.52}W_{0.48}B_2$. Two-dimensional diffraction images at low and high pressure and integration diffraction patterns obtained at the magic angle (φ = 54.7°, effectively hydrostatic conditions) at several pressures are presented for the bulk (Figure 1c,d) and nanoscale samples (Figure 2). Two-dimensional plots evolve from straight lines at low pressure, indicating a hydrostatic stress state, to wavy lines at high pressure, indicating a well-defined high- and low-stress direction. Integrated diffraction patterns at the magic angle smoothly shift to higher angle (smaller lattice constant) with increasing pressure. Note that the pressure for each compression step was derived from the equation-of-state of an internal standard,[41] using its lattice parameter at φ = 54.7°. This explains why the diffraction peaks of Pt are present in the diffraction patterns shown in Figures 1c,d and 2c,d. A small amount of unreacted Re was found in n-ReB_2, as can be seen in Figure 2a,b. Re is also a common pressure standard, like Pt, and its equation-of-state has been well studied.[42−45] As a result, no additional internal standard was needed for this sample.

The data show that the addition of tungsten expands the hexagonal-close-packed metal lattice because W (1.41 Å) is larger than Re (1.37 Å) in atomic size,[46] which causes the peaks to shift toward lower angles in the ambient pressure diffraction data in Figure 2d, compared to the stick reference pattern of ReB_2 (Joint Committee on Powder Diffraction Standards Card #00-006-0541). No pure W phase peaks were observed in the patterns across the entire pressure range, suggesting that WB_2 and ReB_2 do indeed form a solid solution. All diffraction peaks for $Re_{0.52}W_{0.48}B_2$, n-ReB_2, and n-$Re_{0.52}W_{0.48}B_2$ can be cleanly indexed to the ReB_2-type structure. Note that some peaks and the amorphous humps below 10° 2θ (labeled with open stars) do not shift with pressure, and these are from the boron gasket. The background

DOI: 10.1021/acsnano.9b02103
ACS Nano 2019, 13, 10036−10048

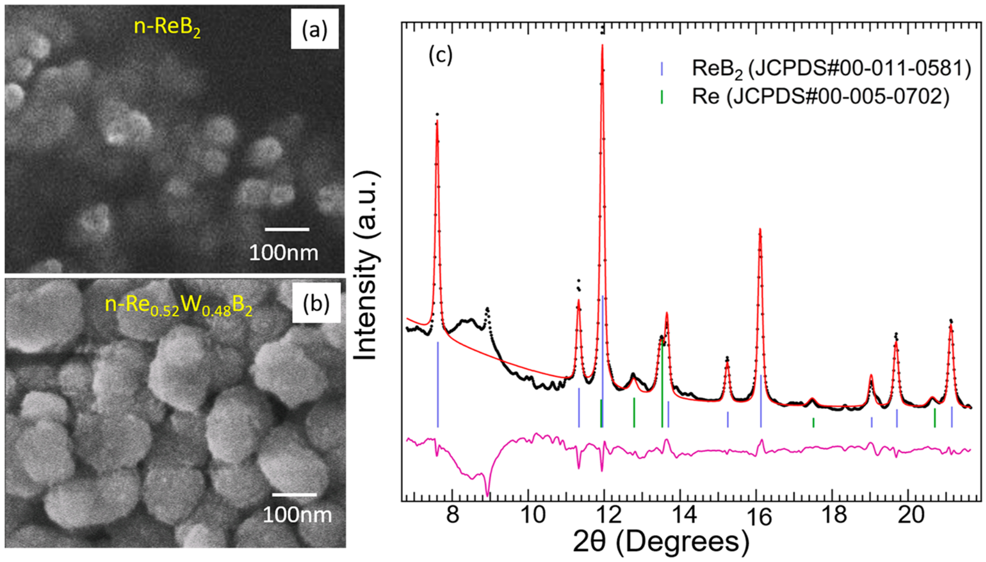

Figure 3. Scanning electron microscopy images of (a) n-ReB_2 and (b) n-$Re_{0.52}W_{0.48}B_2$ prepared using a NaCl flux. Particle sizes range from ∼40 to ∼150 nm for the two samples. (c) Rietveld fitting of nano-ReB_2 at ambient pressure. The experimental spectrum is shown with a black dashed line, and the calculated fit is shown with a solid line in red. The difference pattern is shown in violet. Good agreement is found for all peaks other than those arising from the boron/epoxy gasket.

scan for the gasket alone can be found in Figure S1. There is also a small impurity phase found in the n-$Re_{0.52}W_{0.48}B_2$ sample, which is labeled with a solid star.

All of our bulk samples are prepared by arc melting and are polycrystalline with grain sizes in the micrometer regime. This results in spotty patterns due to the low grain number statistics, as can be seen in Figure 1c,d. The spotty nature of the pattern makes peak intensities unreliable, so that the data cannot be fully refined. In contrast, the diffraction pattern for the sample prepared by NaCl flux growth is smooth, indicating a much finer particle size, which is determined to be between 40 and 150 nm, depending on the sample, as determined by scanning electron microscopy (SEM) (Figure 3a,b). The overall morphology of the nanomaterials can be found in the SEM-EDS images with lower magnification (Figures S2 and S3), showing that the nanomaterials are reasonably monodispersed and tend to form agglomerates. Size histograms extracted from the SEM images for both nanoscale samples are also include in Figure S2 to demonstrate the breadth of the size distribution. The average size from these distributions is ∼50 nm for the n-ReB_2 and ∼120 for the n-$Re_{0.52}W_{0.48}B_2$. We note that only a finite number of SEM images could be collected on more dispersed parts of the powder, so the size statistics from SEM may not fully represent the sample. As a result, we generally use sizes determined form XRD peak widths to describe the samples.

EDS maps demonstrate that Re is found where there are powder grains, indicating that the particles in the SEM images are indeed n-ReB_2. For the n-$Re_{0.52}W_{0.48}B_2$ sample, Re and W colocalize on the EDS maps, again indicating solid-solution behavior. The Si peak in the EDS spectrum of n-ReB_2 arises from the silicon substrate used in the SEM. The peak situated at 3.4 keV appears to be Sn. This is very likely an artifact resulting from the multiple scattering of backscattered electrons, an effect that is very common when performing EDS for uneven surfaces such as powders. The chlorine and sodium peaks found in the spectrum for n-$Re_{0.52}W_{0.48}B_2$ may result from residual salt flux.

The smooth diffraction patterns of n-ReB_2 and n-$Re_{0.52}W_{0.48}B_2$ enabled us to conduct Rietveld refinement, which is a whole pattern refinement technique where the experimental profile is compared with a calculated one.[67] An example of refined data is shown and tabulated in Figure 3c and Table S1. It is known that the peak broadening can be attributed to several factors: instrumental broadening, crystallite size, and stress-induced broadening.[33,47] In our experiments, the instrumental broadening was characterized using a standard material, CeO_2. The Rietveld analysis for the peak profile from the XRD of the unstressed sample shows that the crystallite size for n-ReB_2 and n-$Re_{0.52}W_{0.48}B_2$ is ∼40 nm and ∼30 nm with a microstrain of 0.003 and 0.002, respectively, confirming that the samples are indeed nanosized. Additional broadening at high pressure can be assigned to stress. The size determined by XRD, however, appears to be smaller than that shown in the SEM. This is because SEM measures the particle size rather than the crystallite size. An SEM image of the n-$Re_{0.52}W_{0.48}B_2$ shows that its particle size is 100−150 nm (Figure S2), while XRD shows it is ∼40 nm, which suggests that each particle seen in SEM may be composed of multiple crystalline domains. In comparison, the particle size of n-ReB_2 observed by SEM is close to the crystallite size determined using XRD, indicating that the particles are single domains. As seen in the figure, all diffraction signals including the ReB_2, the unreacted Re, and background were well refined in the Rietveld fitting, with the exception of the amorphous hump from the boron/epoxy gasket.

As can be seen in Figure 4a, a linear variation between the measured *d*-spacings and orientation function $(1-3\cos^2\varphi)$ for the selected lattice planes is observed as expected based on lattice strain theory (eq 2). The hydrostatic *d*-spacings are then determined from the zero intercept of this linear fit, plotted as a function of pressure (Figure 4b). The *d*-spacings show a continuous, linear decrease as the pressure increases with no abrupt changes. This behavior suggests the samples are stable in the hexagonal structure upon compression and decompression up to ∼60, ∼43, and 52 GPa.

DOI: 10.1021/acsnano.9b02103
ACS Nano 2019, 13, 10036−10048

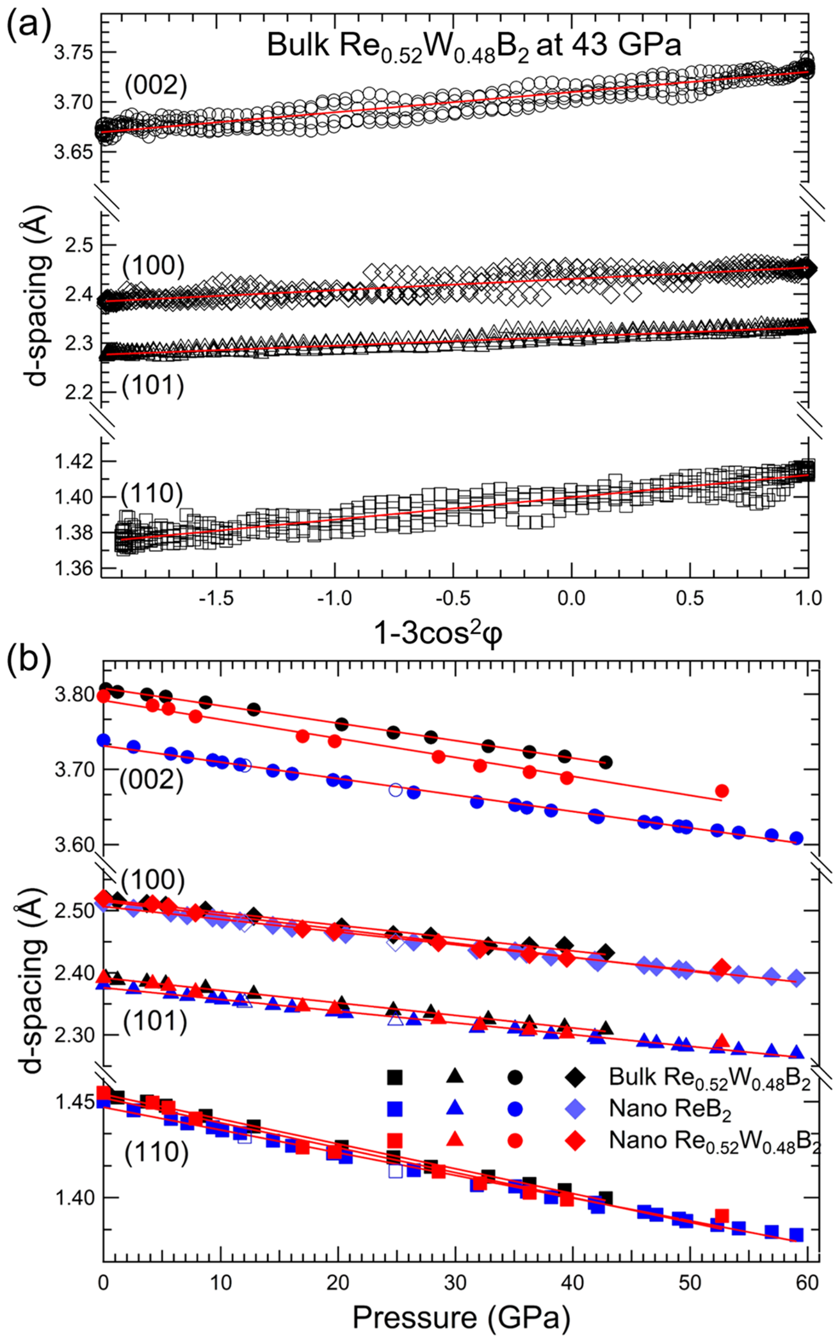

Figure 4. (a) Linearized plot of *d*-spacings for $Re_{0.52}W_{0.48}B_2$ as a function of φ angle at the highest pressure reached. The solid lines are the best linear fit to the data. (b) Measured *d*-spacings for selected lattice planes as a function of pressure. Error bars that are smaller than the size of the symbols have been omitted. Data with close symbols were collected upon compression, while those with open symbols were collected upon decompression. Only the *c*-axis shows large changes upon addition of W to ReB_2.

The lattice parameters at each pressure were calculated from the *d*-spacings and are summarized in Table S2; these data, in turn, enable calculation of the bulk modulus. As shown in Figure 5, the hydrostatic compression curves were fit to the third-order Birch−Murnaghan equation-of-state, yielding a bulk modulus as high as 314 ± 12 GPa ($K_0' = 7.1$), 349 ± 11 GPa ($K_0' = 1.7$), and 326 ± 2 GPa ($K_0' = 4.4$) for bulk $Re_{0.52}W_{0.48}B_2$, n-$Re_{0.52}W_{0.48}B_2$, and n-ReB_2, respectively. The second-order equation-of-state in terms of normalized pressure and Eularian strain[48] can be found in Figure S4. The bulk modulus of n-ReB_2 obtained here under non-hydrostatic compression is consistent with the reported third-order value of 340 GPa for bulk ReB_2 measured under hydrostatic conditions,[6] and it also falls in the range of 317−383 GPa[49−53] obtained from both other experiments and calculations. This indicates that hydrostatic and non-hydrostatic/magic angle data give results in good agreement with each other. Moreover, the fact that the bulk modulus does not change significantly on varying the grain size indicates that the bulk modulus for ReB_2 is a size-independent property. The fact that bulk $Re_{0.52}W_{0.48}B_2$ shows a slightly lower bulk modulus than ReB_2 can be attributed to a decrease in valence electron concentration when substituting W for Re. This decrease, however, seems less significant when determining the bulk

DOI: 10.1021/acsnano.9b02103
ACS Nano 2019, 13, 10036−10048

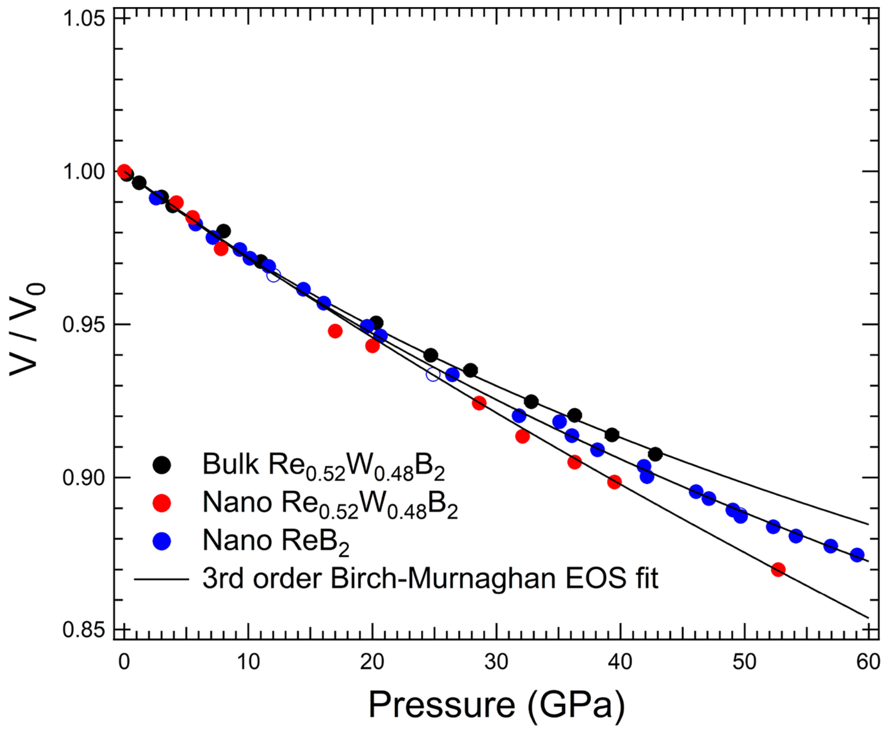

Figure 5. Hydrostatic compression curves of $Re_{0.52}W_{0.48}B_2$ (black), nano-ReB_2 (blue), and nano-$Re_{0.52}W_{0.48}B_2$ (red) obtained at the magic angle, φ = 54.7°. The solid line is the best fit to the third-order Birch−Murnaghan equation-of-state.

modulus of n-$Re_{0.52}W_{0.48}B_2$, since it shows nearly the same bulk modulus value as bulk ReB_2. One possible reason is that the atomic structure of the surface can undergo reconstruction to compensate the energy increase when shifting the atoms from their perfect lattice positions due to the presence of surface strain. It has been found in hard materials such as SiC that the bond distances of Si−C, C−C, and Si−Si at the surface of nanocrystals are different from those within the nanocrystal center, giving rise to a core−shell structure.[54] As a result, the shell shows higher bulk modulus than the inner core. The addition of W decreases the valence electron density, suggesting a lower bulk modulus than ReB_2; however, it may also induce more bonding reconstruction at the surface of the grains, which becomes more significant at the nanoscale, explaining the surprising lack of change in bulk modulus.

Generally, a high bulk modulus (*i.e.*, high incompressibility) is a necessary, but insufficient prerequisite for high hardness.[55] Bulk modulus is a measure of elastic deformation, reflecting the resistance to volume change with respect to pressure, and is strongly related to the intrinsic properties of a material, particularly valence electron count and structure.[56] Hardness, defined as the resistance to plastic deformation, is influenced not only by intrinsic factors such as the strength and directionality of bonding but also by extrinsic factors, such as dislocation density and grain morphology. The yield strength is believed to be one of the most significant determining factors for hardness, and the ratio of yield strength to shear modulus (t/G) for each lattice plane can be directly measured from the slope of the linear fit as shown in Figure 4a. Values of t/G for selected planes are plotted as a function of pressure for bulk $Re_{0.52}W_{0.48}B_2$, n-ReB_2, and n-$Re_{0.52}W_{0.48}B_2$ in Figure 6a,b and compared with data for bulk ReB_2 from ref 57. For n-ReB_2, the t/G ratio for each plane increases almost linearly with pressure from the beginning up to ∼15 GPa. The increase rate then becomes slower and eventually plateaus, indicating the onset of plastic deformation and that t (the yield strength) has reached its limiting value.

Similar trends in t/G are observed for all samples, with some noted differences. In comparing the bulk samples, we find that $Re_{0.52}W_{0.48}B_2$ shows a higher plateau value of t/G and reaches that value at a somewhat higher pressure than pure ReB_2. Similarly, both nanomaterials support a higher plateau value and show a higher plateau pressure compared to their bulk counterparts. Overall, bulk ReB_2 shows both the lowest plateau pressure and plateau value, indicating that all methods used here are successful at improving mechanical properties. As seen in Figure 6a,b the basal plane of the *hcp* lattice for all samples is always the lowest, implying it is very likely to be a slip plane. The $t(100)/G$, $t(101)/G$, and $t(110)/G$ values for n-ReB_2 are quite similar, which we also observed for bulk ReB_2. In contrast, the addition of tungsten seems to change the strain anisotropy. Unlike ReB_2, the planes for $Re_{0.52}W_{0.48}B_2$, in both bulk and nanoscale form, present a significant difference in t/G, with (100) being the highest followed by the (110) and (101) planes. This may relate to the greater sensitivity of the *c*-axis to the addition of tungsten, as shown in Figure 2b,f.

It is important to calculate t, in addition to t/G, when comparing yield strength of different materials, since a very low shear modulus like that found in a soft elastic material can also produce a high strain. For example, the (200) lattice plane of Au[58] can support a similar amount of differential strain to the (004) lattice plane of ReB_2. As described in the Methods section, this conversion can be done making two different limiting assumptions. The Voigt shear modulus assumes iso-strain conditions, while the Reuss shear modulus assumes iso-stress conditions. The differential stress under Reuss and Voigt conditions for bulk and nanoscale $Re_{0.52}W_{0.48}B_2$ and ReB_2 was calculated by using the elastic stiffness constants from refs 59 and 60, respectively. While the real differential stress is a weighted average of these two conditions, the correct

DOI: 10.1021/acsnano.9b02103
ACS Nano 2019, 13, 10036−10048

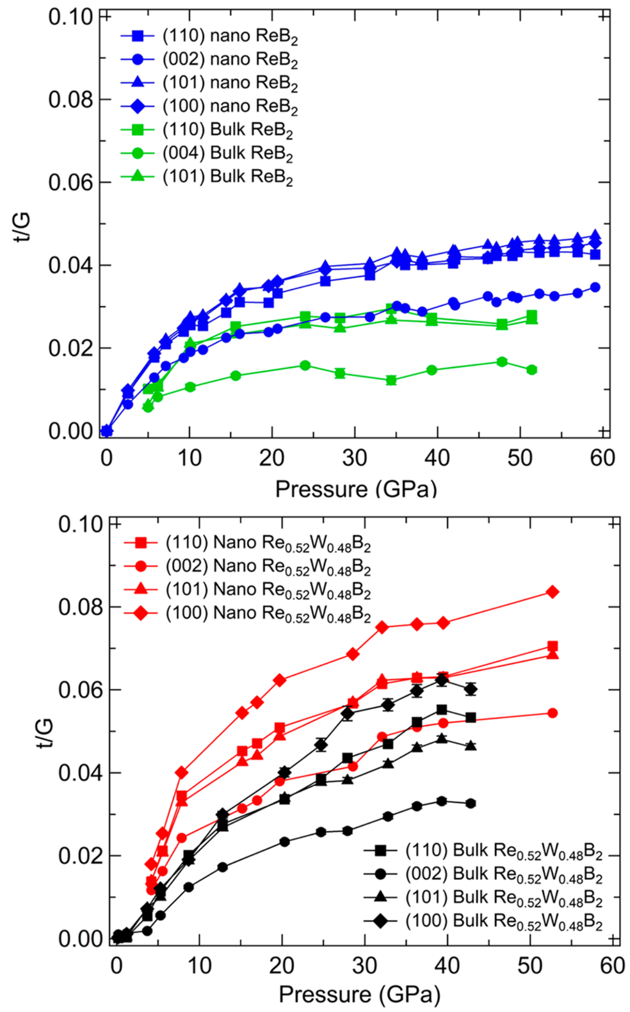

Figure 6. (a) Comparison of the differential strain, given by the ratio of differential stress t to aggregate shear modulus G, as a function of pressure between nano-ReB_2 (blue) and bulk ReB_2 (green). (b) Differential strain as a function of pressure for nano-$Re_{0.52}W_{0.48}B_2$ (red) and bulk $Re_{0.52}W_{0.48}B_2$ (black).

weighting for our experimental conditions is not known, so we simply calculated both values as upper and lower limits on the actual values. As seen in Figure 7a−c, both nanomaterials clearly show higher differential stress values than that of their bulk counterparts. For example, the (100) plane for the $Re_{0.52}W_{0.48}B_2$ system is found to be the strongest plane with a plateau value of ∼16−19 GPa for the bulk material and ∼20−25 GPa for the nanoscale material. The (002) is always the weakest plane regardless of size and composition, again suggesting that this is a slip plane. When comparing different methods to enhance the yield strength, we found the strength for the (002) and (101) planes of n-ReB_2 is almost the same as that of bulk $Re_{0.52}W_{0.48}B_2$. However, the (100) and (110) planes of n-ReB_2 are clearly weaker than those of bulk $Re_{0.52}W_{0.48}B_2$, indicating that bulk $Re_{0.52}W_{0.48}B_2$ possesses an overall higher yield strength than n-ReB_2 and thus that solid-solution effects are more beneficial than finite size effects alone in this system.

Finite size effects are significant, however, as even the weakest plane of n-ReB_2 still exhibits a higher yield strength than the strongest plane of bulk ReB_2, demonstrating that finite size effects are an effective approach to hardness enhancement for superhard metal borides. Because the different lattice planes show more variation in t for $Re_{0.52}W_{0.48}B_2$ then for ReB_2, a clean separation of t values is not observed between bulk and nanoscale $Re_{0.52}W_{0.48}B_2$, but the nanoscale material still shows a significant enhancement in t under both iso-stress and iso-strain assumptions. When the crystallite size is reduced into the nanorealm, the nucleation of dislocations becomes more energetically unfavorable. Moreover, dislocations are also harder to propagate due to the high density of grain boundaries, which in turn is responsible for the higher yield strength of n-ReB_2. Solid-solution effects similarly result in a higher yield strength because dislocation movement is impeded by the atomic size mismatch between tungsten and rhenium. Importantly, it appears to be possible to take advantage of both solid-solution hardening and size effects in a synergistic manner, as n-$Re_{0.52}W_{0.48}B_2$ exhibits the highest differential stress of all samples studied.

In order to correlate the yield strength for a polycrystalline sample to its hardness, the yield strength for many different diffraction planes needs to be considered, because many lattice planes are compressed by the diamond indenter in a polycrystalline material at the same time during the hardness test. While we never know what specific grain orientations are below any given indentation, to get a sense of the average yield strength, here we took the average of all lattice planes that we could track to get an effective average differential stress and plotted the data in Figure 7d. For example, the differential stress of n-ReB_2 shown in Figure 7d was obtained by taking the average of t/G for the (002), (100), (101), (102), (103), (104), (110), and (112) planes followed by multiplying by the aggregate shear modulus of 273 GPa.[60] In Figure 7d, the differential stress for bulk $Re_{0.52}W_{0.48}B_2$ is slightly higher than that for n-ReB_2, and they are both greater than that of bulk ReB_2. This result is consistent with the hardness previously reported for both bulk materials (H_v = 40.5 GPa for bulk ReB_2, H_v = 47.2 GPa for bulk $Re_{0.52}W_{0.48}B_2$).[9] Since n-ReB_2 and n-$Re_{0.52}W_{0.48}B_2$ were made only in powder form, no hardness values are available. However, it is reasonable to believe that the hardness of a compact made from n-ReB_2 should be higher than bulk ReB_2 and close to or slightly lower than bulk $Re_{0.52}W_{0.48}B_2$ based on the differential stress data, while the hardness of a compact made from n-$Re_{0.52}W_{0.48}B_2$ would likely be even higher than the bulk solid-solution value.

We end by taking advantage of our ability to refine the nanocrystal diffraction patterns as a function of pressure to learn more about the available slip systems in these superhard materials. When shear stress is applied to polycrystals, individual grains deform preferentially on slip planes. This results in crystallite rotations, generating lattice-preferred orientation or texture, which manifests as changes in peak intensity with pressure.[61] Unfortunately, the diffraction pattern for the coarse-grained bulk samples (Figure 2a) only allows us to analyze the diffraction line shifts and the evolution of the differential strain upon compression, while peak intensity variation with azimuth angles cannot be correlated to the slip systems because of the low grain number statistics. As a result, in addition to the high strength, another advantage of nanocrystalline samples is that quantitative texture information can be obtained from high-pressure data through Rietveld analysis.

The orientation distribution or texture is represented using an inverse pole figure (IPF), as shown in Figure 8, which denotes the probability of finding the poles (normal) to lattice

DOI: 10.1021/acsnano.9b02103
ACS Nano 2019, 13, 10036−10048

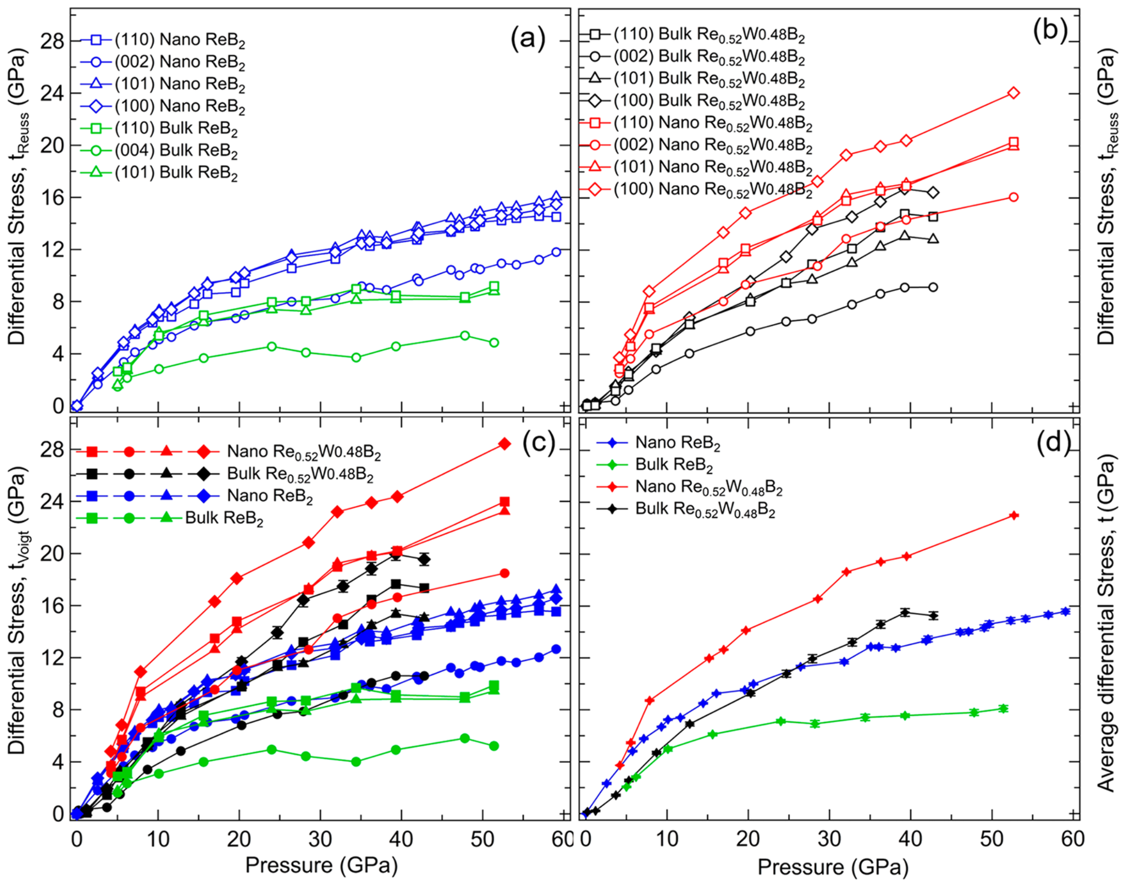

Figure 7. Differential stress (t) calculated under the Reuss (iso-stress) condition (a, b) and Voigt (iso-strain) condition (c). Part (a) compares bulk and nanoscale ReB_2, while part (b) shows bulk and nanoscale $Re_{0.52}W_{0.48}B_2$. Lattice planes are indicated in the figure. Part (c) compares all four samples, and the indexing is the same as that used in parts (a) and (b). Part (d) shows the evolution of the average differential stress over all observed lattice planes with pressure for the same four samples.

planes in the compression direction. The texture strength (*i.e.*, pole density) is measured in multiples of the mean random distribution (m.r.d.), where m.r.d. = 1 indicates a fully random distribution, and a higher m.r.d. number represents stronger texture. The n-ReB_2 initially exhibits a nearly random distribution at ambient pressure. The texture strength evolves with pressure and shows a maximum at (0001) at 59 GPa, indicating the (0001) lattice planes are oriented with an alignment of the *c*-axis to the high-stress direction. This experimental observation confirms that the (001) plane is indeed a slip plane, consistent with our differential stress data and the theoretical slip system of $(001)[1\bar{1}0]$ for ReB_2.[38] As shown in Figure 1, the (001) planes are the planes parallel to the boron layers, and it has been reported that the puckered boron layers become more flattened with increasing pressure;[62] therefore the observed slip plane can be attributed to the lack of constrained bonding between layers.

The preferred orientation for n-$Re_{0.52}W_{0.48}B_2$ was also observed in the (0001) lattice plane, as can be seen in Figure 8b, suggesting that the tungsten added did not change the primary slip system. More interestingly, the texture area (brown in color) for n-ReB_2 grows larger and larger with pressure, implying new slip systems gradually opened up with the development of the plastic deformation. This increase in the number of available slip systems may be the root of the indentation size effect, which is the phenomenon where the measured hardness decreases with increasing indentation load.[5] The indentation size effect is always strongly observed in these superhard metal borides.[9,17,29] Interestingly, the texture for n-$Re_{0.52}W_{0.48}B_2$ is more restricted at the (0001) corner. This suggests that the addition of tungsten helps suppress the formation of new slipping paths, resulting in higher yield strength, greater mechanical stability, and presumably higher hardness.

The quantitative texture strength also provides information about the microscopic deformation mechanisms controlling the plastic behavior of these materials. Dislocation creep and grain boundary processes are believed to be the two main mechanisms for plastic deformation in compressed powders.[63] Dislocation creep on preferred slip systems has been reported to produce a strong texture, while grain boundary sliding and mechanical twinning usually randomize the texture.[35,61,64] Interestingly, both n-ReB_2 and n-$Re_{0.52}W_{0.48}B_2$ exhibit fairly weak texture, with an index of ~1.3 m.r.d. at the highest pressure reached in our experiment, suggesting that the dislocation-mediated processes are not the dominant mechanism for plasticity. Indeed, the low value indicates that the n-ReB_2 and n-$Re_{0.52}W_{0.48}B_2$ maintain a low dislocation density upon non-hydrostatic compression up to ~60 GPa, a result that also explains why the nanomaterials show a much higher yield strength than their coarse-grained counterparts. Importantly for the design of future compacts based on nanocrystalline superhard metal borides, these results also indicate that grain boundary strengthening is the key to enabling high hardness in practical superhard nanoscale metal borides.

DOI: 10.1021/acsnano.9b02103
ACS Nano 2019, 13, 10036−10048

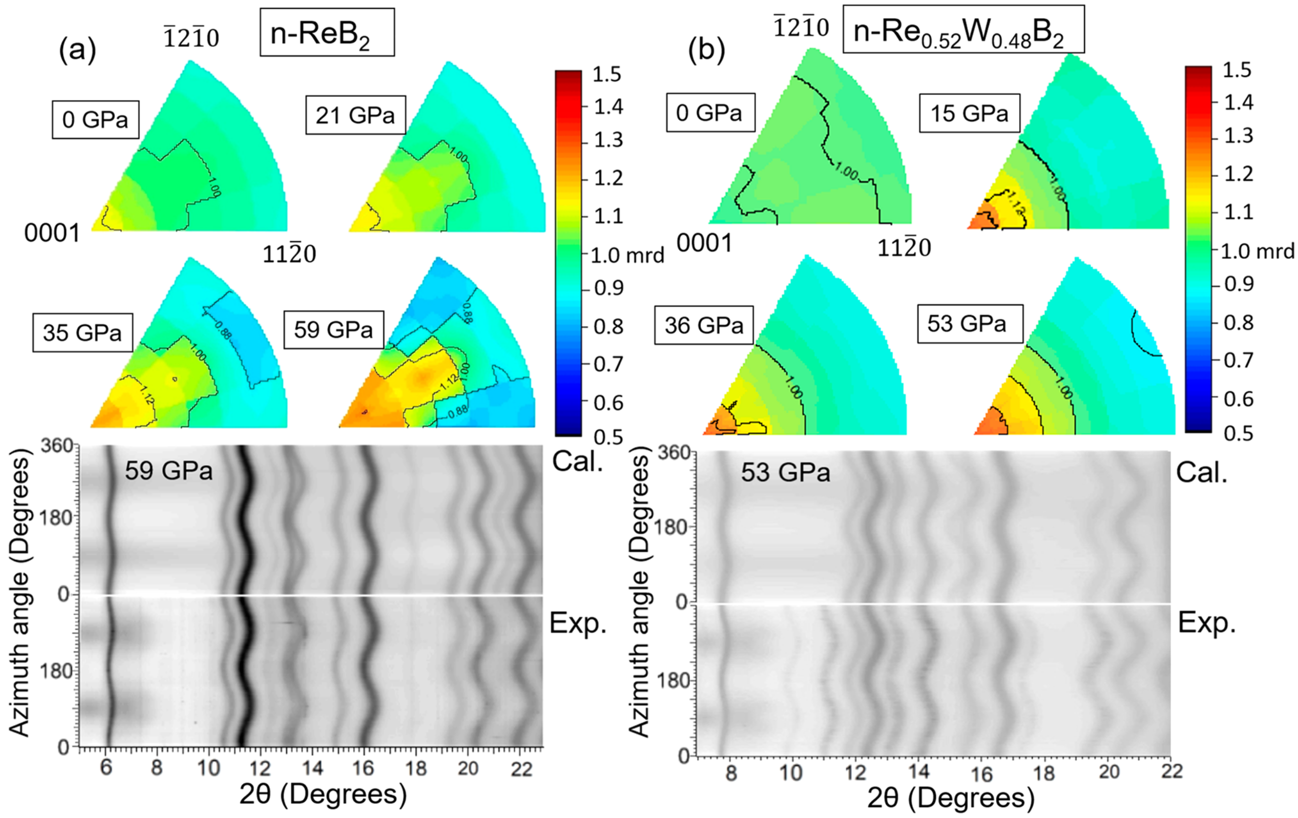

Figure 8. Inverse pole figures for (a) n-ReB_2 and (b) n-$Re_{0.52}W_{0.48}B_2$, showing texture evolution with pressure. Both samples exhibit only weak texture, even when compressed above 50 GPa. For both samples, the (00*l*) direction is found to be the primary slip system. In pure ReB_2, other slip systems become accessible at higher pressures, but these additional slip systems appear to be suppressed in the n-$Re_{0.52}W_{0.48}B_2$.

CONCLUSIONS

In this paper, nanoscale ReB_2 and $Re_{0.52}W_{0.48}B_2$ were synthesized through a molten salt flux growth method. Their high-pressure behaviors were explored and compared with coarse-grained ReB_2 and $Re_{0.52}W_{0.48}B_2$ using synchrotron-based X-ray diffraction under non-hydrostatic compression up to ~60 GPa. The equation-of-state(s) for n-ReB_2, $Re_{0.52}W_{0.48}B_2$, and n-$Re_{0.52}W_{0.48}B_2$ were determined using the hydrostatic volume data measured at the magic angle (φ = 54.7°). Little difference was found in the bulk modulus of n-ReB_2 compared with bulk ReB_2, while nano $Re_{0.52}W_{0.48}B_2$ was found to be more incompressible than bulk $Re_{0.52}W_{0.48}B_2$. Lattice-dependent strength anisotropy indicates that the basal planes of the samples support the least differential stress, indicating that (00*l*) is a slip plane limiting the strength of ReB_2. This hypothesis was further confirmed by texture analysis. Moreover, the yield strengths of bulk $Re_{0.52}W_{0.48}B_2$, n-ReB_2, and n-$Re_{0.52}W_{0.48}B_2$ were all found to be much higher than that of bulk ReB_2, demonstrating that solid-solution hardening and nanostructuring are two effective approaches to hardness enhancement for superhard transition metal borides. Importantly, these two effects can be synergistically combined to produce the highest yield strength in n-$Re_{0.52}W_{0.48}B_2$. Finally, the plastic deformation mechanism for n-ReB_2 and n-$Re_{0.52}W_{0.48}B_2$ was examined, and it was found that the dislocation density remains very low level, despite compression to ~60 GPa.

METHODS

Synthesis of n-ReB_2. Elemental rhenium (99.99%, CERAC Inc., USA) and amorphous boron (99+%, Strem Chemicals, USA) powders were uniformly mixed in the molar ratio Re:B = 1:4 using an agate mortar and pestle. Note that the reaction needs the excess boron to avoid forming lower borides. We then added 100× excess NaCl (99.5%, Sigma-Aldrich, USA) by weight to the mixture and ground for 30 min, followed by transferring into an alumina boat for heat treatment in a tube furnace under flowing argon. The heating profile was set as follows: ramp up to 850 °C over 1.5 h, dwell for another 1.5 h, and then cool down to room temperature over 5 h. Each sample was washed in water and centrifuged several times in order to remove the NaCl. The resulting powders were characterized by powder X-ray diffraction (PXRD) and SEM.

Synthesis of Bulk $Re_{0.52}W_{0.48}B_2$. Bulk $Re_{0.52}W_{0.48}B_2$ was prepared by arc melting. Tungsten and rhenium powders were mixed with amorphous boron at a molar ratio (total metal:boron) of 1:2.25 followed by pressing into pellets. Subsequently, the pellets were arc melted and cooled in argon gas. The synthesis details can be found in ref 9. The ingot was then crushed and ground with a Plattner's-style hardened tool-steel mortar and pestle set (Humboldt Mfg., model H-17270). The resulting powder was sieved with a No. 635 mesh sieve (Humboldt Mfg.) to ensure its particle size is ≤20 μm.

Synthesis of n-$Re_{0.52}W_{0.48}B_2$. Tungsten and rhenium metal powders were mixed and prealloyed in an arc melter. The resultant ingot was then crushed and ground with a Plattner's-style hardened tool-steel mortar and pestle set (Humboldt Mfg., model H-17270). Subsequently, the metal powders were mixed with boron and NaCl following the same experimental procedure used for the n-ReB_2 synthesis.

Synthesis of Bulk ReB_2. Bulk ReB_2 was prepared by arc melting. Rhenium powders were mixed with amorphous boron at a molar ratio of 1:2.05 followed by pressing into pellets. The extra 0.05 mol of

DOI: 10.1021/acsnano.9b02103
ACS Nano 2019, 13, 10036−10048

boron compensates for boron evaporation during arc melting. The pellets were then liquefied in an arc melting furnace under argon gas. The detailed description of the synthesis can be found in a previous report.[8] The ingot was then crushed and ground followed by sieving with a No. 635 mesh sieve (Humboldt Mfg.) to ensure its particle size is ≤20 μm.

Radial X-ray diffraction. The *in situ* angle-dispersive X-ray diffraction experiments under non-hydrostatic pressure were carried out at synchrotron beamline 12.2.2 of the Advanced Light Source (ALS, Lawrence Berkeley National Lab). Nano-ReB_2, bulk $Re_{0.52}W_{0.48}B_2$, and nano-$Re_{0.52}W_{0.48}B_2$ samples were loaded individually into a sample chamber, with a hole drilled by a laser (∼60 μm in diameter) in a boron disc (∼400 μm in diameter and ∼60 μm in thickness), which is made of amorphous boron and epoxy, subsequently embedded in a rectangular Kapton tape.[65] For most samples, a small piece of platinum foil (∼15 μm in diameter) was intentionally placed on top of the sample to serve as an internal pressure standard. No pressure-transmitting medium was added to ensure the presence of non-hydrostatic stress upon compression. More technical details for the DAC may be found in ref 33. In this experiment, the incident monochromatic X-ray beam (25 keV in energy, 20 × 20 μm in beam size) was perpendicular to the loading axis. The diffracted intensity was recorded using an MAR-345 image plate with pressure steps of ∼4 GPa. Calibration of the sample-to-detector distance, beam center, and detector tilt was carried out by using a CeO_2 standard and the program FIT2D.[66] The ring-like diffraction patterns were then "unrolled" into cake diffraction patterns, where azimuthal angle η (with 0° and 180° the low-stress directions and 90° and 270° the high stress directions as shown in Figures 1c and 2a,c) was plotted *versus* 2θ. For bulk $Re_{0.52}W_{0.48}B_2$, the diffraction patterns were imported into Igor Pro (WaveMetrics, Inc.), where each diffraction line was analyzed individually. The diffraction data of n-ReB_2 and n-$Re_{0.52}W_{0.48}B_2$ were analyzed by the Rietveld refinement method[67] as implemented in the software package MAUD.[68]

The combination of radial X-ray diffraction and lattice strain theory[69−71] enabled us to study the stress state of samples under non-hydrostatic compression in a DAC. A set of orthogonal stress components were applied to the sample upon compression. The stress component σ_1 is parallel to the incident X-ray beam, while σ_3 coincides with the loading axis. The difference between σ_1 and σ_3 is termed the uniaxial stress component or differential stress, which is limited by the yield strength of the specimen material according to von Mises yield criterion, eq 1:[72]

$$t = \sigma_3 - \sigma_1 \leq 2\tau = \sigma_y \tag{1}$$

where τ is the shear strength and σ_y is the yield strength. The lattice strain produced by t is given by eq 2:

$$[d_m(hkl) - d_p(hkl)]/d_p(hkl) = (1 - 3\cos^2\varphi)Q(hkl) \tag{2}$$

This equation can be rearranged to a commonly used form as follows:

$$d_m(hkl) = d_p(hkl)[1 + (1 - 3\cos^2\varphi)Q(hkl)] \tag{3}$$

where $d_m(hkl)$ denotes the observed d-spacing in the presence of a deviatoric stress component, while $d_p(hkl)$ is the d-spacing under hydrostatic pressure alone, where φ is the angle between the loading axis and the diffraction plane normal to it.[69−71] Note that the actual stress state of the sample lies between the two extremes determined by the iso-strain[73] and iso-stress[74] conditions; therefore $Q(hkl)$ can be expressed as given in eq 4:

$$Q(hkl) = \left(\frac{t}{3}\right)\{\alpha[2G_R(hkl)]^{-1} + (1 - \alpha)(2G_V)^{-1}\} \tag{4}$$

Here G_V and $G_R(hkl)$ are the Voigt shear modulus (iso-strain) and Reuss shear modulus (iso-stress), respectively. For a hexagonal system, the G_V is given by eq 5:[75]

$$30G_V = 7c_{11} - 5c_{12} - 4c_{13} + 12c_{44} + 2c_{33} \tag{5}$$

The expressions of $G_R(hkl)$ in terms of elastic compliance $[S_{ij}]$ can be found in ref 71. Approximately, the differential stress from eq 4 can be written as

$$t = 6G\langle Q(hkl)\rangle \tag{6}$$

where $\langle Q(hkl)\rangle$ stands for the average value over the observed crystallographic reflections and G is the aggregate shear modulus. Equation 3 indicates a linear relation between $d_m(hkl)$ and $(1-3\cos^2\varphi)$. The slope of the linear fit yields the product $d_p(hkl)Q(hkl)$, which can be used to evaluate and describe contributions of both plastic and elastic deformation.[76,77] The $d_p(hkl)$ obtained from the intercept (with $x = 0$ corresponding to $\varphi = 54.7°$) reflects compression behavior due to the hydrostatic component of stress, which can yield the equivalent hydrostatic compression curve. The zero-pressure bulk modulus, K_0, and pressure derivative can then be determined by fitting the compression curve to the third-order Birch−Murnaghan equation-of-state,[78]

$$P = 1.5K_0\left[\left(\frac{V}{V_0}\right)^{-7/3} - \left(\frac{V}{V_0}\right)^{-5/3}\right]\left\{1 - 0.75(4 - K_0')\left[\left(\frac{V}{V_0}\right)^{-2/3} - 1\right]\right\} \tag{7}$$

Here, the pressure, P, and the unit cell volume, V, are measured at $\varphi = 54.7°$.

ASSOCIATED CONTENT

Supporting Information

The Supporting Information is available free of charge on the ACS Publications website at DOI: 10.1021/acsnano.9b02103.

> XRD pattern of the boron/epoxy gasket; lower magnification scanning electron microscopy images of n-ReB_2 and n-$Re_{0.52}W_{0.48}B_2$ and histograms generated from the images, showing the distribution of nanocrystal sizes; SEM-EDS maps of ReB_2 and $Re_{0.52}W_{0.48}B_2$; W and Re colocate in the elemental maps, indicating alloyed material; normalized pressure *vs* Eularian strain for bulk $Re_{0.52}W_{0.48}B_2$, nano-ReB_2, and nano-$Re_{0.52}W_{0.48}B_2$; lattice parameters and d-spacings for Rietveld fitting of n-ReB_2; compression data for $Re_{0.52}W_{0.48}B_2$, nano-ReB_2, and nano-$Re_{0.52}W_{0.48}B_2$ (PDF)

AUTHOR INFORMATION

Corresponding Authors

*E-mail: tolbert@chem.ucla.edu.

*E-mail: kaner@chem.ucla.edu.

ORCID

Jialin Lei: 0000-0002-3298-8522

Michael T. Yeung: 0000-0002-5677-6970

Richard B. Kaner: 0000-0003-0345-4924

Sarah H. Tolbert: 0000-0001-9969-1582

Notes

The authors declare no competing financial interest.

ACKNOWLEDGMENTS

The authors thank M. Kunz for technical support at the Lawrence Berkeley National Laboratory (LBNL) beamline 12.2.2 and H.-R. Wenk for equipment support. This work was funded by the National Science Foundation under Grant DMR-1506860 (S.H.T. and R.B.K) and the Dr. Myung Ki Hong Endowed Chair in Materials Innovation at UCLA (R.B.K.). Radial diffraction experiments were performed at the Advanced Light Source, beamline 12.2.2 (LBNL). The Advanced Light Source is supported by the Director, Office

DOI: 10.1021/acsnano.9b02103
ACS Nano 2019, 13, 10036−10048

of Science, Office of Basic Energy Sciences, of the U.S. Department of Energy under Contract No. DE-AC02-05CH11231. Partial support for the operation of ALS beamline 12.2.2 is provided by COMPRES, the Consortium for Materials Properties Research in Earth Sciences under NSF Cooperative Agreement EAR-1606856.

REFERENCES

(1) Levine, J. B.; Tolbert, S. H.; Kaner, R. B. Advancements in the Search for Superhard Ultra-Incompressible Metal Borides. *Adv. Funct. Mater.* **2009**, *19*, 3519−3533.
(2) Komanduri, R.; Shaw, M. C. Wear of Synthetic Diamond When Grinding Ferrous Metals. *Nature* **1975**, *255*, 211−213.
(3) Westraadt, J. E.; Sigalas, I.; Neethling, J. H. Characterization of Thermally Degraded Polycrystalline Diamond. *Int. J. Refract. Hard Met.* **2015**, *48*, 286−292.
(4) Taniguchi, T.; Akaishi, M.; Yamaoka, S. Mechanical Properties of Polycrystalline Translucent Cubic Boron Nitride as Characterized by the Vickers Indentation Method. *J. Am. Ceram. Soc.* **1996**, *79*, 547−549.
(5) Chung, H.-Y.; Weinberger, M. B.; Levine, J. B.; Kavner, A.; Yang, J.-M.; Tolbert, S. H.; Kaner, R. B. Synthesis of Ultra-Incompressible Superhard Rhenium Diboride At Ambient Pressure. *Science* **2007**, *316*, 436−439.
(6) Xie, M.; Mohammadi, R.; Mao, Z.; Armentrout, M. M.; Kavner, A.; Kaner, R. B.; Tolbert, S. H. Exploring the High-Pressure Behavior of Superhard Tungsten Tetraboride. *Phys. Rev. B: Condens. Matter Mater. Phys.* **2012**, *85*, No. 064118.
(7) Levine, J. B.; Nguyen, S. L.; Rasool, H. I.; Wright, J. A.; Brown, S. E.; Kaner, R. B. Preparation and Properties of Metallic, Superhard Rhenium Diboride Crystals. *J. Am. Chem. Soc.* **2008**, *130*, 16953−16958.
(8) Chung, H.-Y.; Weinberger, M. B.; Levine, J. B.; Cumberland, R. W.; Kavner, A.; Yang, J.-M.; Tolbert, S. H.; Kaner, R. B. Response to Comment on Synthesis of Ultra-Incompressible Superhard Rhenium Diboride at Ambient Pressure. *Science* **2007**, *318*, 1550.
(9) Lech, A. T.; Turner, C. L.; Lei, J.; Mohammadi, R.; Tolbert, S. H.; Kaner, R. B. Superhard Rhenium/Tungsten Diboride Solid Solutions. *J. Am. Chem. Soc.* **2016**, *138*, 14398−14408.
(10) Yin, S.; He, D.; Xu, C.; Wang, W.; Wang, H.; Li, L.; Zhang, L.; Liu, F.; Liu, P.; Wang, Z.; Meng, C. Hardness and Elastic Moduli of High Pressure Synthesized MoB_2 and WB_2 Compacts. *High Pressure Res.* **2013**, *33*, 409−417.
(11) Hao, X.; Xu, Y.; Wu, Z.; Zhou, D.; Liu, X.; Cao, X.; Meng, J. Low-Compressibility and Hard Materials Reb2 and WB2: Prediction from First-Principles Study. *Phys. Rev. B: Condens. Matter Mater. Phys.* **2006**, *74*, 224112.
(12) Aydin, S.; Simsek, M. First-Principles Calculations of Mnb2, Tcb2, and Reb2 within the Reb2-Type Structure. *Phys. Rev. B: Condens. Matter Mater. Phys.* **2009**, *80*, 134107.
(13) Lazar, P.; Chen, X.-Q.; Podloucky, R. First-Principles Modeling of Hardness in Transition-Metal Diborides. *Phys. Rev. B: Condens. Matter Mater. Phys.* **2009**, *80*, 12103.
(14) Tu, Y.; Wang, Y. First-Principles Study of the Elastic Properties of $Os_xW_{1-x}B_2$ and $Re_xW_{1-x}B_2$ Alloys. *Solid State Commun.* **2011**, *151*, 238−241.
(15) Chen, X.-Q.; Fu, C.; Krčmar, M.; Painter, G. Electronic and Structural Origin of Ultraincompressibility of 5d Transition-Metal Diborides MB_2 (M = W, Re, Os). *Phys. Rev. Lett.* **2008**, *100*, 196403.
(16) Akopov, G.; Yeung, M. T.; Turner, C. L.; Mohammadi, R.; Kaner, R. B. Extrinsic Hardening of Superhard Tungsten Tetraboride Alloys with Group 4 Transition Metals. *J. Am. Chem. Soc.* **2016**, *138*, 5714−5721.
(17) Mohammadi, R.; Lech, A. T.; Xie, M.; Weaver, B. E.; Yeung, M. T.; Tolbert, S. H.; Kaner, R. B. Tungsten Tetraboride, an Inexpensive Superhard Material. *Proc. Natl. Acad. Sci. U. S. A.* **2011**, *108*, 10958−10962.
(18) Chen, B.; Lutker, K.; Raju, S. V.; Yan, J.; Kanitpanyacharoen, W.; Lei, J.; Yang, S.; Wenk, H.-R.; Mao, H.-K.; Williams, Q. Texture of Nanocrystalline Nickel: Probing the Lower Size Limit of Dislocation Activity. *Science* **2012**, *338*, 1448−1451.
(19) Tian, Y.; Xu, B.; Yu, D.; Ma, Y.; Wang, Y.; Jiang, Y.; Hu, W.; Tang, C.; Gao, Y.; Luo, K.; Zhao, Z.; Wang, L.; Wen, B.; He, J.; Liu, Z.; et al. *Nature* **2013**, *493*, 385−388.
(20) Huang, Q.; Yu, D.; Xu, B.; Hu, W.; Ma, Y.; Wang, Y.; Zhao, Z.; Wen, B.; He, J.; Liu, Z.; Tian, Y. Nanotwinned Diamond with Unprecedented Hardness And Stability. *Nature* **2014**, *510*, 250−253.
(21) Jothi, P. R.; Yubuta, K.; Fokwa, B. P. T. A Simple, General Synthetic Route toward Nanoscale Transition Metal Borides. *Adv. Mater.* **2018**, *30*, 1704181.
(22) Portehault, D.; Devi, S.; Beaunier, P.; Gervais, C.; Giordano, C.; Sanchez, C.; Antonietti, M. a General Solution Route toward Metal Boride Nanocrystals. *Angew. Chem., Int. Ed.* **2011**, *50*, 3262−3265.
(23) Hemley, R. J.; Mao, H. K.; Shen, G.; Badro, J.; Gillet, P.; Hanfland, M.; Häusermann, D. X-Ray Imaging of Stress and Strain of Diamond, Iron, and Tungsten at Megabar Pressures. *Science* **1997**, *276*, 1242−1245.
(24) He, D.; Duffy, T. S. X-Ray Diffraction Study of the Static Strength of Tungsten to 69 GPa. *Phys. Rev. B: Condens. Matter Mater. Phys.* **2006**, *73*, 134106.
(25) Duffy, T. S.; Shen, G.; Heinz, D. L.; Shu, J.; Ma, Y.; Mao, H. K.; Hemley, R. J.; Singh, A. K. Lattice Strains in Gold and Rhenium under Nonhydrostatic Compression to 37 GPa. *Phys. Rev. B: Condens. Matter Mater. Phys.* **1999**, *60*, 15063.
(26) Shieh, S. R.; Duffy, T. S.; Li, B. Strength and Elasticity of SiO_2 across the Stishovite−$CaCl_2$-Type Structural Phase Boundary. *Phys. Rev. Lett.* **2002**, *89*, 255507.
(27) Kavner, A.; Duffy, T. S. Elasticity and Rheology of Platinum under High Pressure and Nonhydrostatic Stress. *Phys. Rev. B: Condens. Matter Mater. Phys.* **2003**, *68*, 144101.
(28) He, D.; Shieh, S. R.; Duffy, T. S. Strength and Equation of State of Boron Suboxide from Radial X-Ray Diffraction in a Diamond Cell under Nonhydrostatic Compression. *Phys. Rev. B: Condens. Matter Mater. Phys.* **2004**, *70*, 184121.
(29) Yeung, M. T.; Lei, J.; Mohammadi, R.; Wang, Y.; Tolbert, S. H.; Kaner, R. B. Superhard Monoborides: Hardness Enhancement through Alloying in $W_{1-x}Ta_xB$. *Adv. Mater.* **2016**, *28*, 6993−6998.
(30) Lei, J.; Yeung, M. T.; Robinson, P. J.; Mohammadi, R.; Turner, C. L.; Yan, J.; Kavner, A.; Alexandrova, A. N.; Kaner, R. B.; Tolbert, S. H. Understanding How Bonding Controls Strength Anisotropy in Hard Materials by Comparing the High-Pressure Behavior of Orthorhombic and Tetragonal Tungsten Monoboride. *J. Phys. Chem. C* **2018**, *122*, 5647−5656.
(31) Lei, J.; Chen, B.; Guo, S.; Wang, K.; Tan, L.; Khosravi, E.; Yan, J.; Raju, S.; Yang, S. Structural and Mechanical Stability of Dilute Yttrium Doped Chromium. *Appl. Phys. Lett.* **2013**, *102*, No. 021901.
(32) Mao, W. L.; Struzhkin, V. V.; Baron, A. Q. R.; Tsutsui, S.; Tommaseo, C. E.; Wenk, H.; Hu, M. Y.; Chow, P.; Sturhahn, W.; Shu, J.; Hemley, R. J.; Heinz, D. L.; Mao, H. K. Experimental Determination of the Elasticity of Iron at High Pressure. *J. Geophys. Res.* **2008**, *113*, B09213.
(33) Merkel, S.; Wenk, H. R.; Shu, J.; Shen, G.; Gillet, P.; Mao, H. K.; Hemley, R. J. Deformation of Polycrystalline MgO at Pressures of the Lower Mantle. *J. Geophys. Res.* **2002**, *107*, ECV 3-1−ECV 3-17.
(34) Merkel, S.; Miyajima, N.; Antonangeli, D.; Fiquet, G.; Yagi, T. Lattice Preferred Orientation and Stress in Polycrystalline Hcp-Co Plastically Deformed under High Pressure. *J. Appl. Phys.* **2006**, *100*, No. 023510.
(35) Dorfman, S. M.; Shieh, S. R.; Duffy, T. S. Strength and Texture of Pt Compressed to 63 GPa. *J. Appl. Phys.* **2015**, *117*, No. 065901.
(36) Lei, J.; Yeung, M. T.; Mohammadi, R.; Turner, C. L.; Yan, J.; Kaner, R. B.; Tolbert, S. H. Understanding the Mechanism of Hardness Enhancement in Tantalum-Substituted Tungsten Monoboride Solid Solutions. *J. Appl. Phys.* **2019**, *125*, No. 082529.
(37) Zhang, R. F.; Legut, D.; Niewa, R.; Argon, A. S.; Veprek, S. Shear-induced Structural Transformation and Plasticity in Ultra-

DOI: 10.1021/acsnano.9b02103
ACS Nano 2019, 13, 10036−10048

incompressible Reb2 Limit Its Hardness. *Phys. Rev. B: Condens. Matter Mater. Phys.* **2010**, *82*, 104104.
(38) Zang, C.; Sun, H.; Tse, J. S.; Chen, C. Indentation Strength of Ultraincompressible Rhenium Boride, Carbide, and Nitride from First-Principles Calculations. *Phys. Rev. B: Condens. Matter Mater. Phys.* **2012**, *86*, No. 014108.
(39) Simunek, A. Anisotropy of Hardness from First Principles: The Cases of Reb_2 And OsB_2. *Phys. Rev. B: Condens. Matter Mater. Phys.* **2009**, *80*, No. 060103.
(40) Akopov, G.; Yeung, M. T.; Sobell, Z. C.; Turner, C. L.; Lin, C.; Kaner, R. B. Superhard Mixed Transition Metal Dodecaborides. *Chem. Mater.* **2016**, *28*, 6605.
(41) Fei, Y.; Ricolleau, A.; Frank, M.; Mibe, K.; Shen, G.; Prakapenka, V. Toward an Internally Consistent Pressure Scale. *Proc. Natl. Acad. Sci. U. S. A.* **2007**, *104*, 9182−9186.
(42) Dubrovinsky, L.; Dubrovinskaia, N.; Prakapenka, V. B.; Abakumov, A. M. Implementation of Micro-Ball Nanodiamond Anvils for High-Pressure Studies above 6 Mbar. *Nat. Commun.* **2012**, *3*, 1163.
(43) Anzellini, S.; Dewaele, A.; Occelli, F.; Loubeyre, P.; Mezouar, M. Equation of State of Rhenium and Application for Ultra High Pressure Calibration. *J. Appl. Phys.* **2014**, *115*, No. 043511.
(44) Manghnani, M. H.; Katahara, K.; Fisher, E. S. Ultrasonic Equation of State of Rhenium. *Phys. Rev. B* **1974**, *9*, 1421.
(45) Liu, L. G.; Takahashi, T.; Bassett, W. A. Effect of Pressure and Temperature on the Lattice Parameters of Rhenium. *J. Phys. Chem. Solids* **1970**, *31*, 1345−1351.
(46) Egami, T.; Waseda, Y. Atomic Size Effect on the Formability of Metallic Glasses. *J. Non-Cryst. Solids* **1984**, *64*, 113−134.
(47) Weidner, D. J.; Wang, Y.; Vaughan, M. T. Strength of Diamond. *Science* **1994**, *266*, 419−422.
(48) Meade, C.; Jeanloz, R. Static Compression of $Ca(OH)_2$ at Room Temperature: Observations of Amorphization and Equation of State Measurements to 10.7 GPa. *Geophys. Res. Lett.* **1990**, *17*, 1157−1160.
(49) Koehler, M. R.; Keppens, V.; Sales, B. C.; Jin, R. Y.; Mandrus, D. Elastic Moduli of Superhard Rhenium Diboride. *J. Phys. D: Appl. Phys.* **2009**, *42*, No. 095414.
(50) Suzukia, Y.; Levine, J. B.; Migliori, A.; Garrett, J. D.; Kaner, R. B.; Fanelli, V. R.; Betts, J. B. Rhenium Diboride's Monocrystal Elastic Constants, 308 to 5 K. *J. Acoust. Soc. Am.* **2010**, *127*, 2797.
(51) Wang, Y. X. Elastic and Electronic Properties of TcB_2 and Superhard ReB_2: First-Principles Calculations. *Appl. Phys. Lett.* **2007**, *91*, 101904.
(52) Hao, X. F.; Xu, Y. H.; Wu, Z. J.; Zhou, D. F.; Liu, X. J.; Cao, X. Q.; Meng, J. Low-Compressibility and Hard Materials ReB_2 and WB_2: Prediction from First-Principles Study. *Phys. Rev. B: Condens. Matter Mater. Phys.* **2006**, *74*, 224112.
(53) Chung, H.-Y.; Weinberger, M. B.; Yang, J. M.; Tolbert, S. H.; Kaner, R. B. Correlation between Hardness and Elastic Moduli of the Ultraincompressible Transition Metal Diborides RuB_2, OsB_2, and ReB_2. *Appl. Phys. Lett.* **2008**, *92*, 261904.
(54) Palosz, B.; Stelmakh, S.; Grzanka, E.; Gierlotka, S.; Pielaszek, R.; Bismayer, U.; Werner, S.; Palosz, W. High Pressure X-Ray Diffraction Studies on Nanocrystalline Materials. *J. Phys.: Condens. Matter* **2004**, *16*, 353−377.
(55) Sung, C.-M.; Sung, M. Carbon Nitride and Other Speculative Superhard Materials. *Mater. Chem. Phys.* **1996**, *43*, 1−18.
(56) Yeung, M. T.; Mohammadi, R.; Kaner, R. B. Ultraincompressible. *Annu. Rev. Mater. Res.* **2016**, *46*, 465−485.
(57) Xie, M.; Mohammadi, R.; Turner, C. L.; Kaner, R. B.; Kavner, A.; Tolbert, S. H. Lattice Stress States of Superhard Tungsten Tetraboride from Radial X-Ray Diffraction under Nonhydrostatic Compression. *Phys. Rev. B: Condens. Matter Mater. Phys.* **2014**, *90*, 104104.
(58) Duffy, T. S.; Shen, G.; Shu, J.; Mao, H.; Hemley, R. J.; Singh, A. K. Elasticity, Shear Strength and Equation of State of Molybdenum and Gold from X-Ray Diffraction under Nonhydrostatic Compression to 24 GPa. *J. Appl. Phys.* **1999**, *86*, 6729.
(59) Zhong, M.-M.; Kuang, X.; Wang, Z.-H.; Shao, P.; Ding, L.-P.; Huang, X.-F. Phase Stability, Physical Properties, and Hardness of Transition-Metal Diborides MB_2 (M = Tc, W, Re, and Os): First-Principles Investigations. *J. Phys. Chem. C* **2013**, *2*, 10643−10652.
(60) Levine, J. B.; Betts, J. B.; Garrett, J. D.; Guo, S. Q.; Eng, J. T.; Migliori, A.; Kaner, R. B. Full Elastic Tensor of a Crystal of the Superhard Compound ReB_2. *Acta Mater.* **2010**, *58*, 1530−1535.
(61) Chen, B.; Lutker, K.; Lei, J.; Yan, J.; Yang, S.; Mao, H. Detecting Grain Rotation at the Nanoscale. *Proc. Natl. Acad. Sci. U. S. A.* **2014**, *111*, 3350−3353.
(62) Pellicer-Porres, J.; Segura, A.; Munoz, A.; Polian, A.; Congeduti, A. Bond Length Compressibility in Hard ReB_2 Investigated by X-Ray Absorption under High Pressure. *J. Phys.: Condens. Matter* **2010**, *22*, No. 045701.
(63) Schiotz, J.; Di Tolla, F. D.; Jacobsen, K. W. Softening of Nanocrystalline Metals at Very Small Grain Sizes. *Nature* **1998**, *391*, 561−563.
(64) Zhou, X.; Tamura, N.; Mi, Z.; Lei, J.; Yan, J.; Zhang, L.; Deng, W.; Ke, F.; Yue, B.; Chen, B. Reversal in the Size Dependence of Grain Rotation. *Phys. Rev. Lett.* **2017**, *118*, No. 096101.
(65) Merkel, S.; Yagi, T. X-Ray Transparent Gasket for Diamond Anvil Cell High Pressure Experiments. *Rev. Sci. Instrum.* **2005**, *76*, No. 046109.
(66) Hammersley, A. P.; Svensson, S. O.; Hanfland, M.; Fitch, A. N.; Hausermann, D. Two-Dimensional Detector Software: From Real Detector to Idealised Image or Two-theta Scan. *High Pressure Res.* **1996**, *14*, 235−248.
(67) Rietveld, H. M. a Profile Refinement Method for Nuclear and Magnetic Structures. *J. Appl. Crystallogr.* **1969**, *2*, 65−71.
(68) Lutterotti, L.; Matthies, S.; Wenk, H. R.; Schultz, A. S.; Richardson, J. W. Combined Texture and Structure Analysis of Deformed Limestone from Time-of-Flight Neutron Diffraction Spectra. *J. Appl. Phys.* **1997**, *81*, 594.
(69) Singh, A. K.; Mao, H.-K.; Shu, J.; Hemley, R. J. Estimation of Single-Crystal Elastic Moduli from Polycrystalline X-Ray Diffraction at High Pressure: Application to FeO and Iron. *Phys. Rev. Lett.* **1998**, *80*, 2157.
(70) Singh, A. K. the Lattice Strains in a Specimen (Cubic System) Compressed Nonhydrostatically in an Opposed Anvil Device. *J. Appl. Phys.* **1993**, *73*, 4278−4285.
(71) Singh, A. K.; Balasingh, C.; Mao, H.-K.; Hemley, R. J.; Shu, J. Analysis of Lattice Strains Measured under Nonhydrostatic Pressure. *J. Appl. Phys.* **1998**, *83*, 7567−7575.
(72) Ruoff, A. L. Stress Anisotropy in Opposed Anvil High-Pressure Cells. *J. Appl. Phys.* **1975**, *46*, 1389−1391.
(73) Voigt, W. *Lehrbuch der Kristallphysik*; Teubner Verlag: Wiesbaden, Germany, 1966.
(74) Reuss, A. Calculation of the Centrifugal Limit of Mixed Crystals due to the Plasticity Condition for Single Crystals. *Z. Angew. Math. Mech.* **1929**, *9*, 49−58.
(75) Hearmon, R. F. S. the Elastic Constants of Anisotropic Materials. *Adv. Phys.* **1956**, *5*, 323−382.
(76) Amulele, G. M.; Manghnani, M. H.; Somayazulu, M. Application of Radial X-Ray Diffraction to Determine the Hydrostatic Equation of State and Strength of up to 60 GPa. *J. Appl. Phys.* **2006**, *99*, No. 023522.
(77) He, D. W.; Shieh, S. R.; Duffy, T. S. Strength and Equation of State of Boron Suboxide from Radial X-Ray Diffraction in a Diamond Cell under Nonhydrostatic Compression. *Phys. Rev. B: Condens. Matter Mater. Phys.* **2004**, *70*, 184121.
(78) Birch, F. Finite Strain Isotherm and Velocities for Single-crystal and Polycrystalline NaCl at High Pressures and 300 K. *J. Geophys. Res.* **1978**, *83*, 1257−1268.

DOI: 10.1021/acsnano.9b02103
ACS Nano 2019, 13, 10036−10048